

Comparison of Measured and Numerically Simulated Turbulence Statistics in a Convective Boundary Layer Over Complex Terrain

Raj K. Rai¹ · Larry K. Berg¹ · Branko Kosović² · Jeffrey D. Mirocha³ · Mikhail S. Pekour¹ · William J. Shaw¹

Received: 5 February 2016 / Accepted: 9 November 2016 / Published online: 25 November 2016
© Springer Science+Business Media Dordrecht (outside the USA) 2016

Abstract The Weather Research and Forecasting (WRF) model can be used to simulate atmospheric processes ranging from quasi-global to tens of m in scale. Here we employ large-eddy simulation (LES) using the WRF model, with the LES-domain nested within a mesoscale WRF model domain with grid spacing decreasing from 12.15 km (mesoscale) to 0.03 km (LES). We simulate real-world conditions in the convective planetary boundary layer over an area of complex terrain. The WRF-LES model results are evaluated against observations collected during the US Department of Energy-supported Columbia Basin Wind Energy Study. Comparison of the first- and second-order moments, turbulence spectrum, and probability density function of wind speed shows good agreement between the simulations and observations. One key result is to demonstrate that a systematic methodology needs to be applied to select the grid spacing and refinement ratio used between domains, to avoid having a grid resolution that falls in the grey zone and to minimize artefacts in the WRF-LES model solutions. Furthermore, the WRF-LES model variables show large variability in space and time caused by the complex topography in the LES domain. Analyses of WRF-LES model results show that the flow structures, such as roll vortices and convective cells, vary depending on both the location and time of day as well as the distance from the inflow boundaries.

Keywords Complex terrain · Convective boundary layer · Multiple nesting · Turbulent scales · Weather Research and Forecasting–large-eddy simulation model

Electronic supplementary material The online version of this article (doi:[10.1007/s10546-016-0217-y](https://doi.org/10.1007/s10546-016-0217-y)) contains supplementary material, which is available to authorized users.

✉ Raj K. Rai
raj.rai@pnnl.gov

¹ Pacific Northwest National Laboratory (PNNL), Richland, WA 99352, USA

² National Center for Atmospheric Research (NCAR), Boulder, CO 80307, USA

³ Lawrence Livermore National Laboratory (LLNL), Livermore, CA 94551, USA

1 Introduction

Numerical models that explicitly represent a wide range of spatial scales are useful tools that can improve our understanding of important physical processes that occur within the planetary boundary layer (PBL). In the convective PBL, the mixing of momentum, heat, and moisture is associated with turbulent structures that scale with the PBL depth (e.g., [Stull 1988](#)). The quality of results from numerical models depends on the model representation of the large PBL-scale eddies and the treatment of subgrid-scale (SGS) processes in the model, as well as the accuracy of the lateral boundary forcing used to drive the simulations. Multiple nests with ever-finer horizontal grid spacing can be used to resolve turbulent scales and to include the effect of mesoscale flows on the innermost microscale domain. Therefore, the model solution on the microscale domain [in large-eddy simulation (LES)] also depends on the selection of the horizontal grid spacing and refinement ratio applied between the multiple domains.

LES is a powerful tool that provides insights into turbulent processes over a range of stability in areas of both complex and flat terrain. Most LES studies reported to date have been performed for idealized cases that assume horizontal homogeneity and periodic boundary conditions in the lateral directions, and are limited to a flat homogeneous surface, small symmetric hills, and uneven patches to mimic different surfaces. With the idealized LES set-up, simulations typically use three distinct PBL stability conditions—convective (e.g., [Moeng 1984](#); [Mason 1989](#); [Moeng and Sullivan 1994](#)), stable (e.g., [Moeng and Sullivan 1994](#); [Kosović and Curry 2000](#); [Beare et al. 2006](#)), and neutral (e.g., [Porté-Agel et al. 2000](#); [Bou-Zeid et al. 2004](#); [Chow et al. 2005](#)). In addition to the use of LES to investigate atmospheric processes, highly resolved LES has also been employed in wind-energy applications for investigating the generation of power and wakes in wind farms ([Calaf et al. 2010](#); [Porté-Agel et al. 2011](#); [Churchfield et al. 2012](#); [Aitken et al. 2014](#); [Mirocha et al. 2014a](#)), and for assessing wind-turbine performance ([Rai et al. 2016](#)) under neutral PBL conditions. In recent years, the Weather Research and Forecasting (WRF) model framework ([Skamarock et al. 2008](#)) has been used, initially developed for forecasting of mesoscale weather features, for idealized LES applications. As with other LES codes, the WRF-LES model has been used to study the behaviour of the PBL under different stability conditions and to implement and develop new turbulence parametrizations ([Noh et al. 2003](#)). These efforts have included idealized LES in the study of turbulence in a case with two-way nesting ([Moeng et al. 2007](#)), and implementation of a non-linear SGS model ([Mirocha et al. 2010](#)).

Application of LES to real-world cases requires time-varying boundary conditions, an approach that generally uses multiple nested domains that downsize the grid spacing from mesoscale (\sim km) to microscale (\sim m). For one real case, [Talbot et al. \(2012\)](#) used multiple nested domains (three WRF model mesoscale and three LES mode) using grid spacings as fine as 50 m. Similarly, [Liu et al. \(2011\)](#) used a multiple nesting approach in WRF real-time four-dimensional data assimilation LES to nest down from 30 km to \approx 100 m grid spacing for wind-energy applications. The innermost LES domain of these two real case studies is defined to have relatively flat terrain. Similarly, these studies do not discuss the methodology used to select appropriate boundary condition in the LES domain nor do they provide a detailed evaluation of the resolved turbulence.

Downscaling of mesoscale simulations to LES scales is made more difficult because of the so-called ‘grey zone’ ([Wyngaard 2004](#)), which relates to the region where turbulent eddies are simultaneously poorly resolved and where the grid spacing is too fine for standard turbulence parametrizations. In this region, the WRF model may be unable to average over sufficient

energy-containing eddies, upon which the PBL parametrization in the WRF model is based. On the other hand, the grid spacing for the LES is relatively large, such that modelled SGS terms do not account for the modelled energy correctly. [Zhou et al. \(2014\)](#) investigated the grey zone by performing simulations with varying grid spacing (from mesoscale to LES scale) for convective boundary-layer (CBL) cases and pointed out the physical and dynamical problem of the grey zone. [Ching et al. \(2014\)](#) also analyzed high-resolution mesoscale simulations of the CBL and argued that the emerging convective structures found in mesoscale simulations with grid spacing in the grey zone are numerical artefacts. They explored modifications to a PBL parametrization that suppresses the development of such artefacts while more accurately representing turbulent fluxes. In addition to issues related to the grey zone, the development of turbulence near the edge of the LES domain is another area of difficulty, depending on a number of factors, including the atmospheric stability and the complexity of the terrain. [Mirocha et al. \(2014b\)](#) introduced a perturbation method that was improved and generalized by [Muñoz-Esparza et al. \(2014\)](#).

Our study employs the state-of-the-art WRF model framework to simulate conditions for a real convective case in an area of complex terrain. Multiple nests of WRF model domains are employed for downscaling the grid spacing from the outermost mesoscale domain (horizontal grid spacing of 12.15 km) to the finest LES domain (horizontal grid spacing 30 m). The study explores the effect of horizontal grid spacing on the solution of mesoscale models by maintaining the domain size constant and varying the grid spacing between 2.7 and 0.8 km. We apply LES to a region of complex terrain that includes the Columbia Basin Wind Energy Study (CBWES) field site ([Berg et al. 2012](#)) and the simulation results are compared to observations from the field study. The results are evaluated with observations in terms of first- and second-order statistical moments, and there is good agreement between the LES and observations. Similarly, we briefly analyze the different flow structures associated with atmospheric stability, terrain features, and computational domain size. In the subsequent discussion, Sect. 2 presents the method used to generate the variables both for WRF-mesoscale and WRF-LES model domains. A method for selection of the appropriate spatial grid spacing in the mesoscale domain that provides forcing to the LES domain is presented in Sect. 3. The LES results are analyzed in Sect. 4 and the WRF-LES model is shown to accurately simulate the mean velocity and variance of the velocity fluctuations as well as underlying distributions and turbulent spectra.

2 Methods

This section describes the configuration of WRF model version 3.6.1 used herein, and provides a brief overview of the observations used to evaluate the simulation. A total of six WRF model domains are used—three mesoscale and three LES.

2.1 WRF Model Simulation in Mesoscale Mode

The mesoscale domains were used to provide time-varying boundary conditions to the LES domains. The three outer mesoscale domains (i.e., D01, D02, and D03) are centred at 45.9551°N and -118.6877°W (Fig. 1a), which is also the location of the tower used during CBWES ([Berg et al. 2012](#)). The outermost domain, D01, encompasses an area of approximately $2000 \times 2000 \text{ km}^2$ and uses a horizontal grid spacing of 12.15 km. The inner domains, D02 and D03, decrease the horizontal grid spacing by factors of three and consist of an equal number of grid points as that of domain D01 (i.e., 166). In the present study, any mesoscale domain with a horizontal grid spacing smaller than 1.2 km produced an artefact

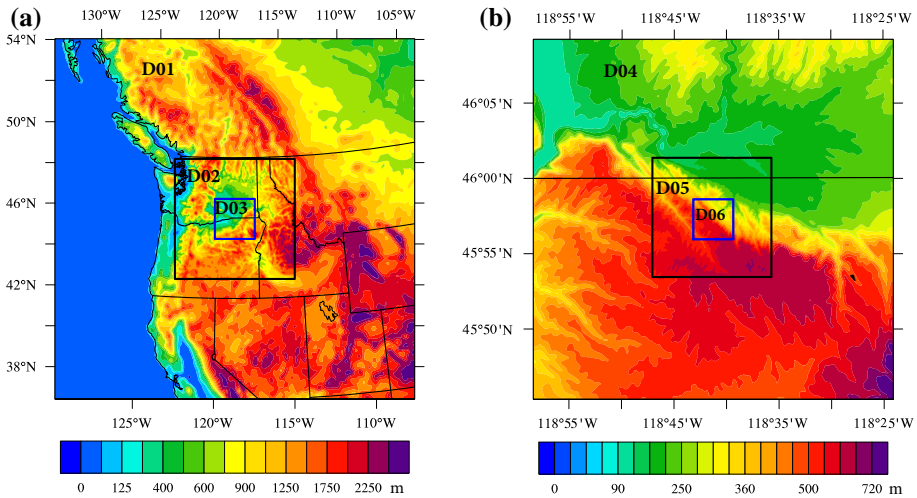


Fig. 1 Computational domain for **a** mesoscale simulations (D01, D02, and D03), and **b** microscale simulations (D04, D05, and D06) with the terrain elevation and state boundaries

in the WRF-mesoscale model solution. A detailed analysis of the methods used to select the horizontal grid spacing in the three mesoscale domains is discussed below. All WRF model domains consist of equal numbers of vertical levels; the vertical grid spacing increases with altitude, but the grid is configured such that the aspect ratio is approximately unity within the boundary layer. The detailed procedure used to assign the number of vertical layers is discussed below.

Two PBL schemes have been applied in the mesoscale simulations—the local 1.5-order closure turbulent kinetic energy (TKE)-based MYNN2 scheme (Nakanishi and Niino 2006) and the non-local first-order closure YSU scheme (Hong et al. 2006). These two schemes represent common parametrization approaches. The YSU scheme is non-local and parametrizes profiles of mixing within the PBL based on bulk PBL characteristics, while the MYNN scheme is local and bases mixing on prognostic subgrid TKE. Similarly, two surface-layer schemes, MYNN and MM5 Monin–Obukhov, are used herein. As applied in the WRF model, the YSU scheme uses the latter surface-layer scheme, whereas the MYNN scheme uses either surface-layer scheme. The initial and boundary conditions for the mesoscale domains were derived from the North American Regional Reanalysis (Mesinger et al. 2006) that is available at a 3-h interval and uses a 32-km horizontal grid spacing. Additional details in regard to the model configuration and physics packages used in the mesoscale simulation are presented in Table 1. For the sake of brevity, the mesoscale simulations completed using the WRF model platform are henceforth termed ‘WRF-Meso’ simulations.

2.2 WRF Model Simulation in LES Mode

The three microscale domains shown in Fig. 1b are nested inside the innermost WRF-Meso domain D03 so that all six domains share a common centre point, i.e., the location of the CBWES site. The ratio of the grid refinement between the WRF-Meso domain D03 and microscale domain D04 is 5, whereas the grid-refinement ratio between any two consecutive WRF-Meso or microscale model domains is 3. For the sake of brevity, the microscale simulations in the WRF model framework are henceforth termed WRF-LES simulations.

Table 1 Data and schemes used in WRF-Meso and WRF-LES models

| | |
|---|---|
| PBL schemes | YSU (Hong et al. 2006) MYNN (Nakanishi and Niino 2006) |
| Radiation scheme | RRTMG (Iacono et al. 2008) |
| Microphysics | Morrison 2-mom (Morrison et al. 2009) |
| Surface-layer schemes | MYNN, MM5 Monin–Obukhov |
| Land-surface model | Noah (Chen and Dudhia 2001) |
| Geographic data (horizontal resolution) | |
| Elevation | Mesoscale : 5 min, 2 min, 30 s Microscale: 1 s |
| Land use | Microscale and mesoscale: 5 min, 2 min, 30 s |

Table 2 Domain size, grid spacing, and timestep used in the WRF-Meso and WRF-LES model simulations

| Model | Domain | $n_x = n_y$ | n_z | $\Delta x, y$ (km) | Δt (s) |
|----------|--------|-------------|-------|--------------------|----------------|
| WRF-Meso | D01 | 166 | 140 | 12.15 | 15 |
| | D02 | 166 | 140 | 4.05 | 5 |
| | D03 | 166 | 140 | 1.35 | 5/3 |
| WRF-LES | D04 | 166 | 140 | 0.27 | 1/3 |
| | D05 | 166 | 140 | 0.09 | 1/9 |
| | D06 | 166 | 140 | 0.03 | 1/27 |

The reason for applying a large grid refinement (i.e., 5) between the domains is to downsize the horizontal grid spacing as rapidly as possible so as to minimize the number of domains within the grey zone. The horizontal grid spacings used for the domains D04, D05, and D06 are 270, 90, and 30 m, respectively. Other combinations of grid refinement could also be used to produce highly resolved grid spacings in the WRF-LES model domain. However, users should consider a number of different factors when selecting the grid spacing, including: the limitation of vertical grid spacing near the surface, the targeted aspect ratio between horizontal and vertical grid spacing, the grey zone, and computational resources.

The boundary-layer depth simulated in preliminary WRF-Meso model runs was used for assigning the vertical grid spacing applied in the WRF-LES model. Our preference is to maintain fine vertical grid spacing within the PBL, to capture as wide a range of motions as possible over the depth of the boundary layer. It is also optimal to use an aspect ratio ≤ 1 in the innermost WRF-LES model domain. This provision requires that the coarsest vertical grid spacing be comparable to the horizontal grid spacing within the PBL. In this case, the minimum vertical grid spacing near the surface was ≈ 16 m and the horizontal grid spacing in the innermost LES domain was 30 m; a uniform vertical grid (≈ 16 m) is applied within approximately 300 m of the surface. The grid was then stretched, ranging from approximately 16 to 30 m below an altitude of 2 km. Above 2 km the vertical grid spacing increases from approximately 30 m to 0.95 km at the model top. The WRF-LES model domain employs the same number of grid points and vertical levels as the mesoscale model (Table 2). The relevant physics schemes and sub-models, such as the surface-layer scheme and the land-surface model, were the same in the two domain types. High-resolution (31-m grid spacing) topographic data were used on the LES domains, while 1-km data were used in the innermost WRF-Meso model domain. However, the land-cover data used for WRF-LES model domains were derived from the same 30-arcsec data used in the WRF-Meso model simulation.

The YSU and MYNN PBL parametrization schemes were used to model the turbulence in the grid column of the mesoscale simulation. These parametrizations were not used in the WRF-LES model simulations, which employ a 3-D turbulence model to parametrize the

SGS turbulence. We used the TKE 1.5-order closure model for modelling SGS motions, which, in addition to the length scale and model coefficient, also computes the SGS TKE as a prognostic variable to predict the eddy viscosity (Lilly 1967). Previously, a perturbation method has been applied (Muñoz-Esparza et al. 2014) to expedite the turbulence generation and may further reduce the influence of the inflow boundary in the simulation. However, the results from our simulations showed that turbulence develops rapidly within the innermost LES domain during the afternoon, which may be due to the complex terrain with variable land cover used within that domain. Therefore, perturbation methods were not used herein, though they should be part of a robust, general downscaling framework.

Simulations on all six domains were run concurrently (online) using one-way nesting between the mesoscale and LES domains, in contrast to Talbot et al. (2012), who used an offline nesting simulation approach. In both online and offline one-way nesting, the parent domain does not use any information from nested domain and the two approaches may produce similar results. However, the online one-way nesting approach is essentially faster than the offline method because all domains run concurrently. The WRF-Meso model simulation was performed for 27 h, beginning from 0000 UTC [0600 Pacific Standard Time (PST)] on 10 May 2011. The WRF-LES model simulation began 15 h into the run to allow for spin-up of the WRF-Meso model simulation. The results from WRF-LES model domains D04, D05, and D06 were saved every 4, 3, and 2 s, respectively, whereas the results from WRF-Meso model domain were only saved every 30 min. Thus, the simulations provide 12 h of results for all six domains during typical cloud-free unstable daytime conditions.

2.3 Observations

Data used to evaluate the WRF-LES model results were collected as part of CBWES. In situ measurements of wind speed, wind direction, and turbulence were made using three tower-mounted sonic anemometers (Applied Technologies, Inc., SATI/3K) at two heights (one at 30 m, two at 60 m) above the surface. The sonics were deployed using three booms 3.5 m in length attached to an existing open-lattice tower. Orthogonal wind components and virtual temperature data were available from the sonic anemometers with the sampling frequency of 10 Hz. The details of observations are described by Berg et al. (2012). The second set of data includes the composite vertical wind profile constructed from a Vaisala Inc., 915 mHz radar wind profiler (provided by the US Department of Energy Atmospheric Radiation Measurement Facility), a Scintec MFAS Doppler sodar, and propeller and vane anemometers mounted on the tower maintained by the Bonneville Power Administration. Data from all devices were combined into the single best estimate of the wind profile as described in Berg et al. (2012). The same dataset was used by Yang et al. (2013) to evaluate a suite of WRF-Meso model simulations.

3 Selection of Spatial Resolution

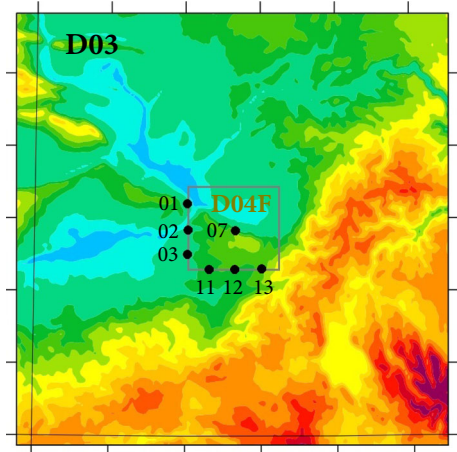
Before presenting the WRF-LES model results and their comparison with the CBWES data, we discuss the horizontal grid spacing used in the WRF-Meso model runs and its impact on the model solution. This approach of investigating the effects of horizontal grid spacing on the simulation results is intended to provide a better estimate of the boundary forcing for the WRF-LES model, while limiting the impact of issues related to the grey zone.

The WRF-Meso model domains provide the boundary forcing to the outermost WRF-LES model domain; therefore, the accuracy of WRF-LES model results depends, at least

Table 3 Cases for WRF-Meso model simulations with varying horizontal resolution and number of grid points

| Run | $n_x = n_y$ | n_z | $\Delta x, y$ (km) | | |
|-----|-------------|-------|--------------------|-----|-----|
| | | | D01 | D02 | D03 |
| W1 | 82 | 140 | 24.3 | 8.1 | 2.7 |
| W2 | 94 | 140 | 21.6 | 7.2 | 2.4 |
| W3 | 106 | 140 | 18.9 | 6.3 | 2.1 |
| W4 | 124 | 140 | 16.2 | 5.4 | 1.8 |
| W5 | 142 | 140 | 14.4 | 4.8 | 1.6 |
| W6 | 160 | 140 | 12.6 | 4.2 | 1.4 |
| W7 | 184 | 140 | 10.8 | 3.6 | 1.2 |
| W8 | 226 | 140 | 9.0 | 3.0 | 1.0 |
| W9 | 280 | 140 | 7.2 | 2.4 | 0.8 |

Fig. 2 WRF-Meso model domain D03 containing the fictitious domain D04F (grey box) and seven locations to extract the vertical profiles of wind speed and temperature (black dots)



in part, on the accuracy of the forcing obtained from the WRF-Meso model simulation. We investigate the impact of spatial resolution on the WRF-Meso model simulation results by comparing a number of WRF-Meso model simulations that use varying horizontal grid spacing (i.e., cases W1–W9 presented in Table 3). Similar simulations were performed by Zhou et al. (2014) for studying the grey zone and its impact on their simulations, but they maintained a constant number of grid points and varied the grid spacing for a single domain. Here, all cases have similar domain size—approximately the size of domains portrayed in Fig. 1a, and in each configuration, the same physics and dynamics options as well as the same boundary and initial conditions are applied. However, the horizontal grid spacing and number of grid points are different in each case. For example, the grid spacing in both x and y directions in domain D03 varies from 2.7 km in the first case to 0.8 km in the ninth case, and the grid refinement between each of the three domains was kept at 3. In order to study the effect of spatial resolution on the WRF-Meso model results, conditions at the boundary of an imaginary WRF-LES model are considered (Fig. 2). This pseudo-domain D04F occupies an area equivalent to the WRF-LES model domain D04. The solid dots in the western face (i.e., 01, 02, and 03), southern face (i.e., 11, 12, and 13), and centre (i.e., 07) of the rectangular boundary line represent the locations from which vertical profiles of wind speed and temperature are saved at every timestep for subsequent analysis. The solid dots in the western and southern boundary faces are approximately 13 km apart.

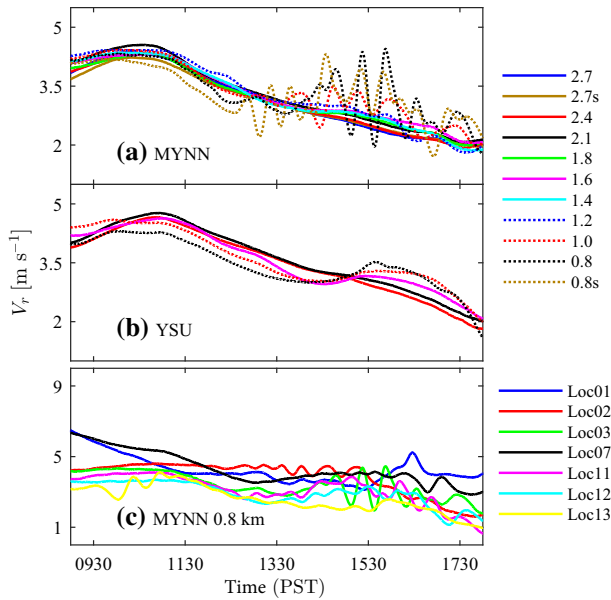
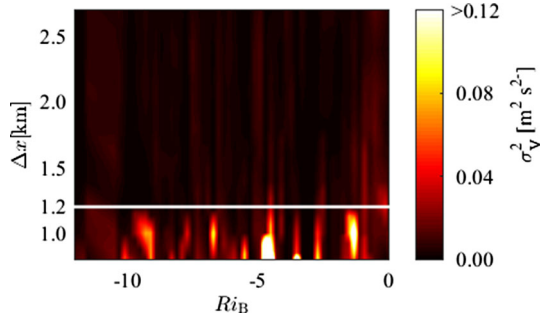


Fig. 3 Time series of resultant velocity obtained from locations of western and southern boundaries and middle of fictitious domain D04F (in Fig. 2) for **a** MYNN PBL scheme and **b** YSU PBL scheme. The legend with ‘0.8s’ indicates the WRF model simulation that uses the MM5 Monin–Obukhov surface-layer and MYNN PBL schemes. Time series derived from all seven locations for grid spacing 800 m using the MYNN PBL scheme is shown in **c**. For all cases, the velocities are used from the location ≈ 90 m above the surface

Using the simulated data from the centre of domain D03, the time series of the resultant velocity (i.e., $\sqrt{u^2 + v^2 + w^2}$) have been constructed at a height 90 m above the surface using the results of both PBL parametrization schemes—MYNN (Fig. 3a) and YSU (Fig. 3b). The results obtained from the WRF-Meso model using the MYNN PBL parametrization scheme shows that the simulated wind speed becomes oscillatory during the afternoon for all horizontal grid spacing < 1.2 km. Similarly, the results from the WRF-Meso model using the YSU PBL scheme also show deviations of the wind speed for all grid spacings < 1.2 km—noting that the changes are more gradual but not oscillatory as seen in the MYNN PBL scheme. This suggests that, for both PBL schemes employed, when specifying spatial resolution in the mesoscale domain, the horizontal grid spacing should not be < 1.2 km to avoid generating numerical artefacts in the model solution. Note that the surface-layer representation used in the MYNN PBL and YSU PBL schemes in WRF-Meso model simulations are MYNN and MM5 Monin–Obukhov, respectively. To further investigate the sensitivity of the surface-layer scheme on the WRF-Meso model results, additional simulations for 0.8- and 2.7-km grid spacing (subscript with s in Fig. 3a) with the MYNN PBL parametrization were run using the MM5 M–O surface-layer scheme. The result with the MM5 M–O surface-layer scheme shows similar oscillations to the cases run with the MYNN surface-layer scheme. In addition, time series from seven different locations (Fig. 3c) of the fictitious domain D04F also produce similar behaviour during the afternoon when the boundary-layer depth increases. At coarser resolution, the results are similar for both PBL schemes. A more detailed study is required to determine the exact causes of the oscillations that occur in the simulations with the spatial resolution < 1.2 km (on the order of the boundary-layer depth) during the afternoon. One potential cause of such an oscillation may be related to numerical artefacts

Fig. 4 Variance of wind speed against the bulk Richardson number Ri_B and horizontal grid spacing Δx . The *white line* is used to demarcate the high-variance zone from the low-variance zone



associated with grid spacing within the grey zone. Alternatively, the oscillatory behaviour may result from unrealistic structures in the simulated flow. For example, [Ching et al. \(2014\)](#) found that convectively-induced secondary circulations, such as rolls found in the mesoscale simulation, depend on grid spacing and PBL schemes. Although our simulations are better behaved in the morning (local time) with no oscillations, there is still a large amount of variability even among those with the coarser grid spacing. Only two cases with coarser grid spacing (i.e., 2.7 and 2.4 km) showed similar behaviour over the entire simulation period. The results of WRF-Meso model simulations with varying spatial resolutions suggest that a careful selection of the horizontal grid spacing must be considered in order to provide the best possible boundary forcing to the LES domain.

The effect of horizontal spatial resolution on the model solution was also examined in terms of the atmospheric stability using the profiles from six locations lying along the western face (i.e., 01, 02, and 03) and southern face (i.e., 11, 12, and 13) of the imaginary boundary (Fig. 2). At each location, the bulk Richardson number (Ri_B) was calculated over 30-min intervals for grid spacings ranging from 2.7 to 1.8 km. To calculate Ri_B , the variables (wind speed, temperature) from the first three model layers ($\approx 8, 24,$ and 40 m) above the surface were used, with gradients calculated using the variables from 8 and 40 m; the mean temperature was taken from a middle location. The results from finer resolution simulations (grid spacing < 1.8 km) were not used when calculating Ri_B to avoid an erroneous solution due to the oscillations in the wind speed. However, the wind-speed variance was calculated using 30-min data at ≈ 90 m above the surface using the entire range of grid spacing (i.e., 0.8 to 2.7 km). For the simulation results obtained using the MYNN PBL scheme, Fig. 4 depicts the wind-speed variance for different stability conditions and horizontal grid spacing. The results show that the largest variances are found for horizontal grid spacing < 1.2 km over the entire range of Ri_B shown. The white line corresponds to a 1.2-km grid spacing and also demarcates areas of high and low variance. The discontinuities of the variances found in the higher-resolution region can be attributed to the relatively small sample size, and a longer simulation would help fill these gaps. This suggests that the WRF-Meso model with finer grid spacing may produce unrealistic simulations regardless of the static stability. The critical grid spacing may depend on the topography and/or PBL depth. As suggested from this analysis, we applied the 1.35-km horizontal grid spacing in the innermost WRF-Meso model domain.

The WRF-Meso model simulations were also used to investigate the growth of the daytime boundary layer. The PBL depth at the centre of the domain D03 was calculated from the WRF-Meso model simulations that used the MYNN scheme, and is shown in Fig. 5 for the cases W1 through W9. Similarly, the PBL depth has been estimated from sodar-returned signal data and from the radar wind profiler's signal-to-noise ratio (Fig. 5); the basic principles of both

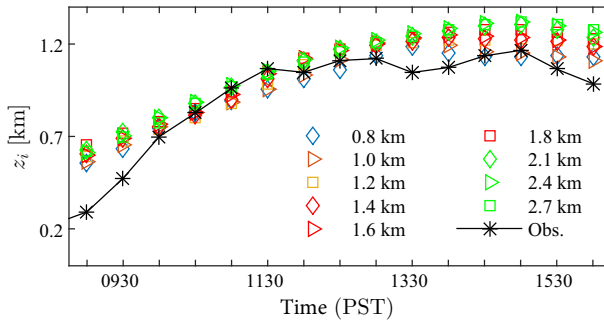


Fig. 5 Boundary-layer depth from a WRF-Meso model simulation and observed data at the centre of the domain D03

retrievals are discussed in [Beyrich \(1997\)](#) and [Seibert et al. \(2000\)](#). There is generally good agreement in the simulated and observed PBL depths over the course of the simulation, with the maximum simulated PBL depth on the order of 1 km. The results also show that WRF-Meso model simulations with grid spacing < 1.2 km have systematically low boundary-layer depths during the afternoon. One explanation for the oscillatory behaviour observed in [Fig. 3](#) for WRF-Meso model simulations with higher resolution may be related to the PBL depth. It is expected that the size of the convective eddies scale with the boundary-layer depth, which is ≈ 1 km in this case. Furthermore, the PBL parametrization applied in the WRF-Meso model simulation is based on the concept of ensemble averaging within the PBL parametrization, which requires at least several eddies to be present within the grid cell. In this case, when using horizontal grid spacing < 1.2 km in the WRF-Meso model simulation, the concept of ensemble averaging may not be valid; at the same time, the WRF-Meso model simulation resolve some of the largest eddies, although the representation is expected to be quite poor. This explanation suggests one reason for the oscillatory behaviour seen in WRF-Meso model runs. Furthermore, this behaviour is most obvious when the boundary layer is relatively deep and wind speed is small. Similar results were found in [Ching et al. \(2014\)](#) and [Zhou et al. \(2014\)](#).

4 Results and Discussion

Here, we present the analysis of the LES results and observations. In the first two subsections, comparisons of the simulated and measured variables including spectra and first- and second-order statistical moments are presented. A brief discussion of the spatial and temporal variabilities for the mean and variance quantities is also provided.

4.1 Instantaneous and Mean Quantities

The temporal snapshot of a variable, such as wind speed, at a given instant provides an interesting perspective of the simulated field at that time. [Figure 6](#) shows wind velocity along the three vertical planes from LES domain D06 at 1300 PST for the three orthogonal wind components (u , v , w) viewed from along and across the predominant flow direction and from the top of the domain. Each panel in the top two rows represent the velocity component for vertical planes passing diagonally $c - c'$ and $m - n$. Similarly, the panels in the bottom row show the planar view of the sixth model level (≈ 90 m) viewed from the top. The lines in

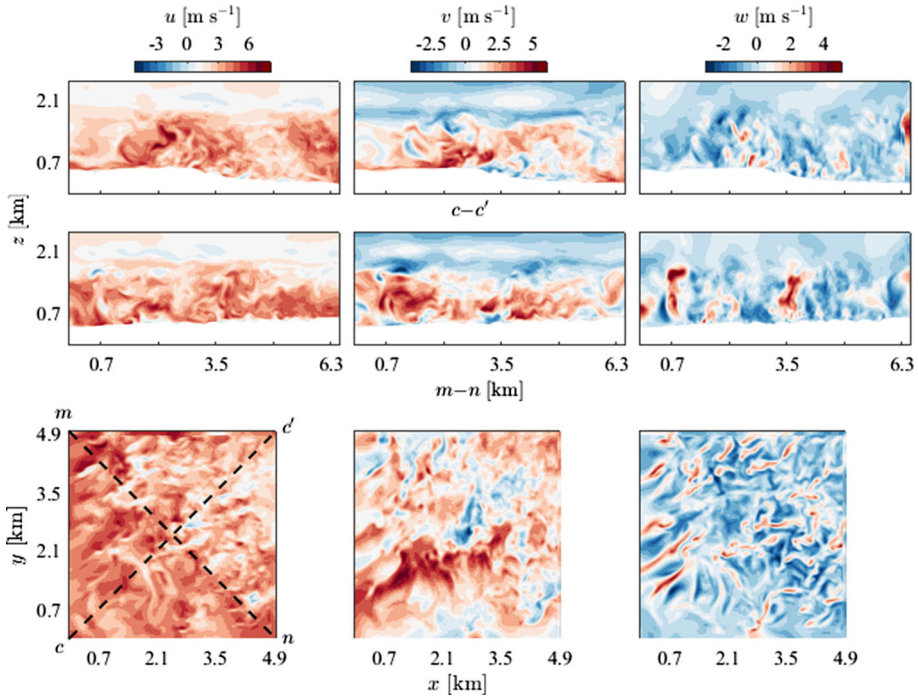


Fig. 6 Instantaneous velocity components [u (left column), v (middle column), and w (right column)] showing for domain D06 in the vertical inflow planes passing through diagonals $c - c'$ (first row) and $m - n$ (second row), and in a terrain-following xy plane passing through the sixth model layer (third row) at 1300 PST. The dashed lines in the first panel of the third row show the diagonals $c - c'$ and $m - n$

the bottom left panel show the orientation of the vertical planes. In all three planar xy plots, turbulent structures can be observed throughout most of the domain. However, the nature of the turbulence structures differ, with those in the south-western corner being generally larger and more linear than those in the north-eastern corner. The predominant wind is south-westerly during this case study and the ridge lies approximately along the diagonal $m - n$ direction, perpendicular to the mean flow. The region downstream from the ridge (i.e., north-eastern region) has lower elevation than the upstream region. Because of this predominant flow direction and terrain elevation changes, the middle panel for $c - c'$ inflow planes (shown in the top row of Fig. 6) shows a wake region (velocity deficit) downstream from the ridge. Furthermore, the spatial structures of the wind components become finer in the wake region than in its surroundings. On the other hand, the vertical cross-section passing through $m - n$ in the middle row shows more homogeneous structures throughout the plane, as the terrain elevation does not vary much along this transect and given the mean wind direction (across the ridge). Strong updraft and downdrafts associated with thermals can be seen in the right panel. Overall, the vertical wind component shows that the flow is highly convective. Visual inspection of the figure reveals that the most intense turbulence is found in the north-eastern region of the domain, which is characterized by low elevation compared to other areas of domain D06. A detailed discussion on the features of turbulence follows in sub-Sect. 4.2.

The convergence statistics for the wind data (see “Online Resource”) shows that their first- and second-order moments converge in 30 min. Therefore, the simulated and observed

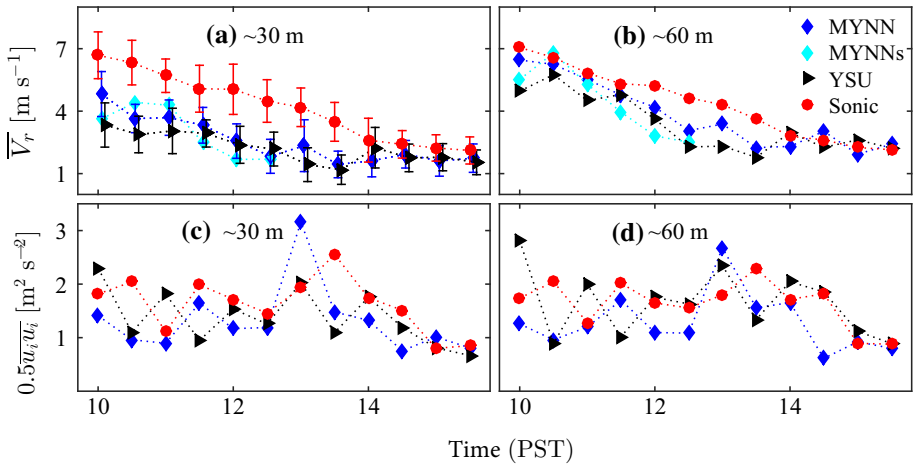


Fig. 7 Comparison between the time series derived from 30-min averaged LES-generated and sonic-measured wind speed (a, b), and TKE (c, d) at two different heights. The LES data at 24 m and 56 m above the surface is compared with sonic data at 30 and 60 m above t , respectively

mean wind speeds were calculated over 30-min intervals for the daytime period (1000–1600 PST) from the sonic at the centre of domain D06. The simulation results from the centre of the domain were driven by two independent WRF-Meso model runs using either the MYNN or YSU PBL scheme. For brevity, the two different LES solutions are termed WRF-LES(MYNN) and WRF-LES(YSU). Figure 7a, b shows the comparison of mean wind speed between the MYNN and YSU schemes for the WRF-LES model results and the sonic data at heights of 30 m and 60 m. A comparison of the simulated and observed wind speeds show that they follow a similar trend—a decrease of wind speed in the afternoon. However, the simulated mean wind speed at a height of 60 m agrees better with the observed data compared to the result at a height of 30 m. Using the MM5 M–O surface-layer scheme in the WRF-LES(MYNN) model simulation (i.e., legend with suffix s in Fig. 7), the time series of wind speed for 1000–1300 PST also shows differences compared to the results found using the MYNN surface-layer scheme. This indicates that the WRF-LES model result is sensitive to the surface-layer scheme, but that the application of either scheme does not lead to an improvement in the simulated wind speed. To evaluate the temporal variability in the simulated and observed wind speed, the error bars for the wind speed were derived from each 30-min data for a height of 30 m. It shows that the variability decreases in both simulated and observed wind speeds as time progresses. Similarly, error bars computed for a height of 60 m also show similar variability (not shown here). The vertical profile of wind speed and direction over different times (see “Online Resource”) also reveal similar agreement between the simulated and observed data. In addition to the mean wind speed, the TKE ($0.5 \overline{u_i u_i}$) was calculated for the period of 1000–1600 PST (Fig. 7c, d) for the same height ranges used in the analysis of mean wind speed. The TKE from the WRF-LES model is derived using both the resolved wind field and SGS stress terms. The result shows that $0.5 \overline{u_i u_i}$ between the simulated and measured values (Fig. 7c, d) scatters in the range of $2 \text{ m}^2 \text{ s}^{-2}$ over this time period at both heights (i.e., 30 and 60 m). Overall, the discrepancies seen between the observation and simulation may result from many factors, such as the numerical scheme, parametrization used, and boundary forcing. Note that the comparison made herein is for a single point, over a limited period of time. Additional investigation is needed to determine

if the use of a specific PBL parametrization for the WRF-Meso model simulations leads to improved LES results.

4.2 Turbulence Characterization

LES can be used to simulate the motion of turbulent eddies within the boundary layer. The average TKE discussed earlier provides a snapshot of the amount of turbulence in the flow, but does not provide information about the temporal scales of turbulence. We employ the autospectral density function to the time series of wind speed to present the turbulence in the frequency domain. For the k th block of data, the autospectral density function of the quantity x is expressed as $S_{xx}^k = X^*(f)X(f) T^{-1}$, where X^* is the complex conjugate of X , T is the time period for the k th block of the data, and f is the frequency in Hz. A multistep process was used to construct the autospectral density function as follows: seven separate 30-min time series (i.e., blocks of data), each separated by 15 min, were considered for a 2-h period ranging from 1200–1400 PST. This resulted in separate time series constructed from time periods 1200–1230, 1215–1245 and so on. The 15 min of overlap between the 30-min time series provided seven spectra to be averaged, and helped to remove noise from the spectra and obtain a smoother autospectral density function. Figure 8a–c show the autospectral density function for three wind components, u , v , and w , for the observed and simulated wind speeds at the centre of domain D06. The time series data were taken from heights of ≈ 60 m for the WRF-LES model and 60 m for sonic data. In each panel, spectra are shown for the WRF-LES(MYNN) and WRF-LES(YSU) simulations for each domain D04, D05, and D06 (that apply 270, 90, and 30 m horizontal grid spacing, respectively). The other spectra are constructed from the observed data and the inclined line represents a $-5/3$ slope line. Both WRF-LES(MYNN) and WRF-LES(YSU) results and sonic data have used 0.5-Hz sampling frequency (recall that the 0.5-Hz sonic data was created from an original 10-Hz data stream). The LES results show that, for all three velocity components, with the exception of the lower-resolution cases and in the lower frequency region, the amount of turbulence resolved in each domain (i.e., D04, D05, and D06) by WRF-LES(MYNN) and WRF-LES(YSU) simulation is similar. As expected, the results show that the vertical velocity component exhibits less power than the horizontal velocity components, and the varying amounts of turbulence are resolved in the WRF-LES model with different grid cell sizes. The simulation with the smallest grid spacing is able to resolve the largest amount of turbulence. For example, the spectra

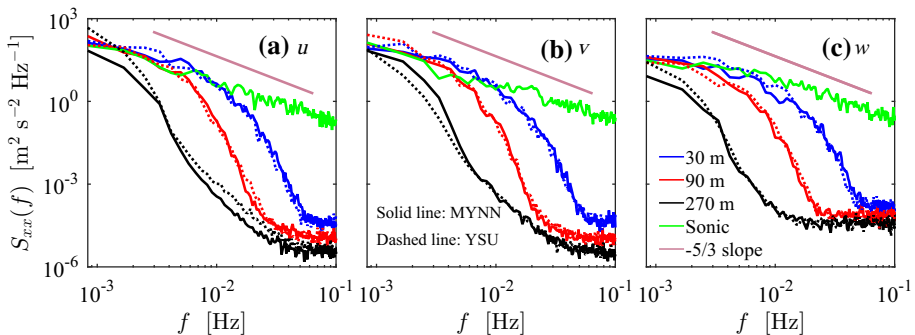


Fig. 8 Autospectral density function for the three wind components **a** u , **b** v , and **c** w for the LES-generated wind field with three spatial resolutions and sonic measurement data. The autospectral density function is constructed from data for the time period of 1200–1400 PST

from the WRF-LES model with 30-m spatial resolution began to roll off for frequencies >0.018 Hz, followed by frequencies that are nearly multiples of three for 90 and 270 m resolution cases (consistent with the changing grid spacing). Given the average wind speed of approximately 4 m s^{-1} during this period, and together with the effective resolution of the WRF model (i.e., up to $7\Delta x$) (Skamarock 2004), the highest frequency range that the WRF-LES model is expected to capture is approximately 0.019 Hz for the 30-m spatial resolution and its multiple of three for simulations using 90- and 270-m resolution cases. The results demonstrate that the WRF-LES model has captured nearly the same amount of turbulence as the effective resolution of the model allows. Keeping in mind that the spectra from both WRF-LES model results are similar and the overall better prediction of TKE and mean wind speed by WRF-LES(MYNN) in this case study, the subsequent WRF-LES model results presented in discussions are from only the WRF-LES(MYNN) simulation.

The development of turbulence in the simulation varies in both time and space, and depends on many factors, such as surface thermal forcing, terrain, boundary conditions, fetch distance, wind speeds, spin-up time. To illustrate the development of turbulence in the WRF-LES model domains, plots of the instantaneous vertical wind component at the 20th model layer (i.e., ≈ 300 m above surface) for three LES domains are presented in Fig. 9. The five panels in the bottom row show the terrain elevation for the three WRF-LES model domains, D04, D05, and D06, and for the domains D04E1 (D04-Extended 1) and D04E2 (D04-Extended 2), which have the same grid spacing of domain D04 but with area extended to the south-west by 33% and by 66% to the western and southern sides of domain D04. Three reference locations are highlighted in the bottom left panel of Fig. 9 with letters W, C, and E that represent the western, central, and eastern locations from which the vertical profiles are extracted from the simulations for additional analysis. The centre location, C, corresponds to the location of the CBWES tower. Locations W and E are 660 m from the west and east of the boundary of domain D06. The panels in the top three rows of the three rightmost columns represent the planar view at three instantaneous times 1000 PST (first row), 1200 PST (second row), and 1400 PST (third row) for domains D04, D05, and D06. The results show that the flow structures vary in both space and time. The south-western region is occupied by long streak-like structures, whereas the north-eastern region is filled with smaller turbulent cell-like structures. The streak-like structures appear as the roll vortices that are aligned in the direction of mean wind speed. During the late morning (from 1000 to 1200 PST), the wind speed is found to be moderate ($\approx 7 \text{ m s}^{-1}$ at 90 m above the surface) and there is also moderate heat flux (approximately 300 W m^{-2}) from the surface. The combination of heat flux and wind shear favours the formation of convective rolls (Moeng and Sullivan 1994) in the south-western region. The roll wavelength is found to be $\approx 3 \text{ km}$ ($\approx 3z_i$) at 1200 PST, similar to the simulation of shear and convective turbulent flow by Moeng and Sullivan (1994). Weckwerth et al. (1997) suggested that the roll wavelength changes with PBL depth and the surface heat flux. However, here the orientation of the roll changes with variations in the mean wind speed, but a similar roll wavelength is maintained over an extended time interval even after the flow becomes more convective. In addition to the change in the orientation of the rolls, the area occupied by the rolls also decreases (most evident in D04) as time progresses due to the decrease of wind speed throughout the afternoon, and that the sensible heat flux remain small. The number of rolls associated with the parent domain also wanes as the spatial resolution in the nested domain increases (e.g., in D06 from D05). As a result, the majority of the domain is occupied by small-scale structures that were only found in the north-eastern corner of the domain before 1200 PST. The value of $-z_i/L$ (L is the Obukhov length) is found to be approximately 2 (the median value for a period of 1300–1330 PST). This value is consistent for rolls with the range of $-z_i/L$ described by Deardorff (1972), Grossman (1982), and Sykes

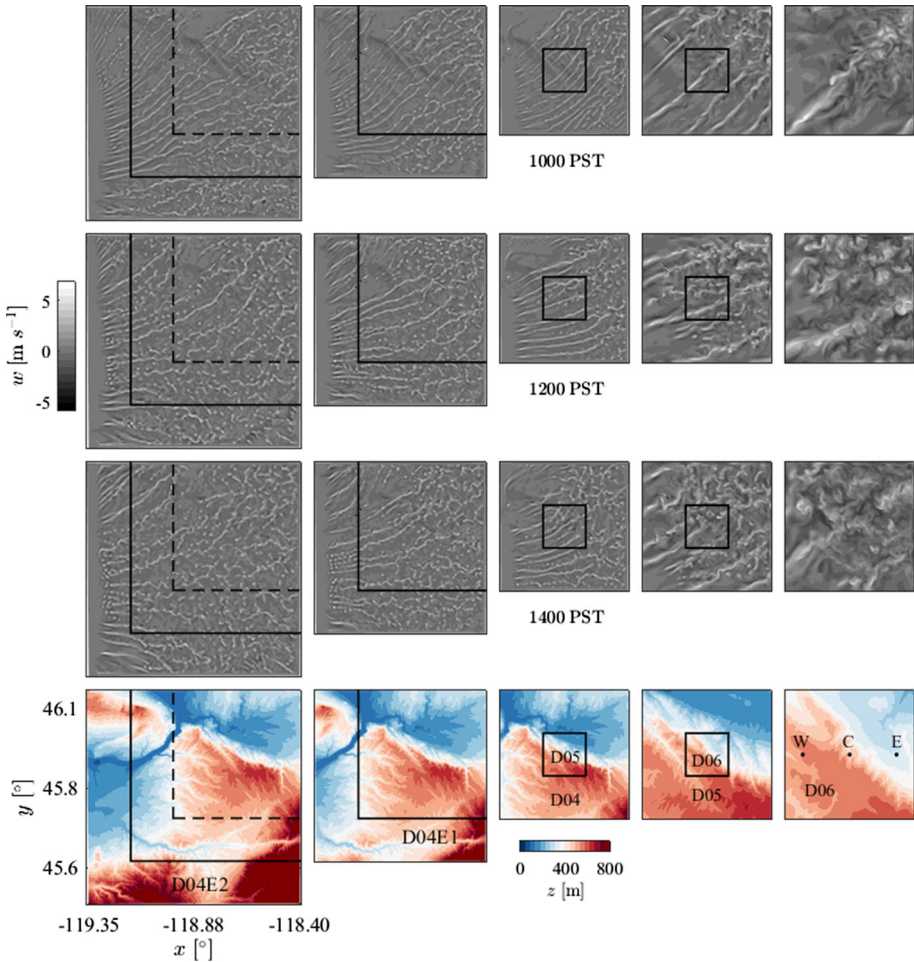


Fig. 9 Terrain elevation of LES domains D04, D04E1, D04E2, D05, and D06 (*bottom row*) and contours of vertical wind component at 20th model layer (≈ 300 m above the surface) drawn for three instantaneous times 1000, 1200, and 1400 PST (*top three rows*). The domains D04E1 and D04E2 are the domains extended by 33 and 66% along the south and west directions of domain D04

and Henn (1989), but is slightly smaller than that found by LeMone (1973). Weckwerth et al. (1997) found rolls for values of $-z_i/L$ as large as 57.

The structure of the roll vortices and the transition to cellular convection in the simulations may be affected by the proximity of the upwind edge of the domain. To investigate this impact, the LES domain D04 was extended along the south-west and has been named D04E1 and D04E2 (the extended length of the domain is shown by solid and dashed lines in Fig. 9). The domains D04E1 and D04E2 receive boundary forcing from the innermost WRF-Meso model domain D03, similar to the original domain D04. Snapshots from the extended domains are presented in the first and second column from the left. Compared with results from domain D04, the results from extended domain D04E1 and D04E2 at 1000 PST reveal no significant differences in the development of convection roll structures within domain D04 in either case. During this time, the wind speed in the south-western corner of the domain is higher

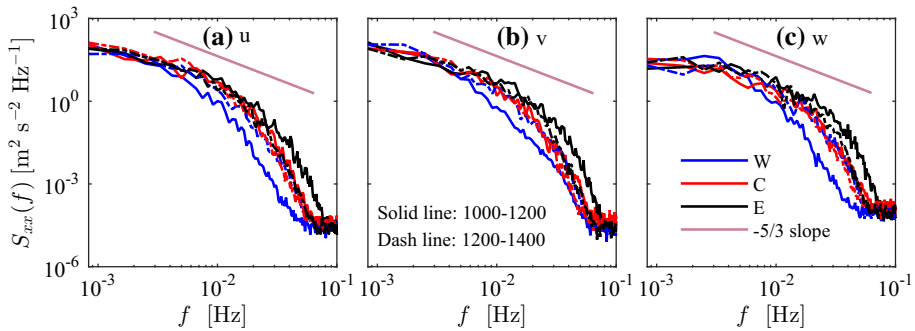


Fig. 10 Spectra of the three velocity components derived from the LES data for domain D06 at three spatial locations and two periods: 1000–1200 PST and 1200–1400 PST

($\approx 7 \text{ m s}^{-1}$) and the heat flux is moderate ($\approx 300 \text{ W m}^{-2}$). Flow in the north-eastern part of the domains has small-scale turbulent structures associated with the presence of the ridge and relatively low terrain where wind speed is smaller. The combination of wind speed, heat flux, and topography found at 1000 PST helps to sustain roll vortices in the south-western region and open convective cells in the north-eastern region even for the extended domains D04E1 and D04E2. However, at later times (1200 and 1400 PST), the flow structures in the part of domain D04 that is within domains D04E1 and D04E2 (shown by dashed lines in Fig. 9) changes gradually. By 1400 PST, the south-western region of domain D04 within D04E1 is mostly, and the area within D04E2 entirely, covered by open cells. As the day progresses, the flow loses its streak-like features and the domain is filled with small structures. This result reveals that the turbulent structures within the area of interest depends on the distance from the inflow boundaries. This also suggests that the roll structures that appear in the original domain D04 in the later times (i.e., 1200 and 1400 PST) may be attributed to numerical treatment rather than real physical process. However, an instantaneous snapshot shown here might not reveal all the details of the flow, and should be verified by observations. Nevertheless, the analysis has used data from the innermost LES domain D06, as the details of flow associated with D04 do not have a large impact on D06.

A qualitative study of the results shown in Fig. 9 demonstrates that the amount of turbulence in the simulation varies both in space and time. For a quantitative study, the spectrum of turbulence from the three representative locations W, C, and E of domain D06 (shown in the bottom right panel of Fig. 9), for the two periods 1000–1200 and 1200–1400 PST, is examined. Figure 10 displays the spectra derived from the time series of three velocity components at the three locations for the two time periods. The left panel shows the spectra for locations W, C, and E derived from the u component of wind velocity for the time periods 1000–1200 PST (solid lines) and 1200–1400 PST (dashed lines). The results indicate that the magnitude of the turbulence at location W is less than that observed at other locations. For location W, the spectra begin to roll off at lower frequencies signifying less turbulence associated with small-scale features during the time 1000–1200 PST. However, for the same period, the turbulence in locations C and E is more intense and extends to smaller scales. Location W lies in the region where the flow structures are characterized by convective rolls during the period 1000–1200 PST (Fig. 9). The distance between the roll structures is observed at a distance of $\approx 3z_i$, so any individual point in the model domain might not be within a roll vortex at any particular time. The distance of the W location from the boundary is 690 m and the simulated turbulence might still be increasing in intensity. Therefore the reduced turbulence seen at W

location could be both—position of W relative to the rolls and distance from the boundary (spin-up issue of turbulence). As a result, it appears that only the lowest frequencies are captured near the inflow boundary. An examination of the instantaneous velocity variance (not shown) does show pockets of increased variance at discrete locations within the domain, and highlights the fact that rolls lead to increased heterogeneity in resolved turbulence. Later in the day, from 1200–1400 PST, turbulence at point W increases to match the conditions at locations C and E, consistent with the transition to cellular convection across the domain.

4.3 Spatial and Temporal Variability

In addition to spectra, probability density functions (p.d.f.s) can also be used to characterize turbulence variability. The p.d.f.s derived from the velocity time series at location C for different periods are shown in Fig. 11a–c. For each period, four individual p.d.f.s were constructed using 30 min of observed or simulated wind-speed fluctuations and then averaged together. The kurtosis (i.e., relative sharpness) shows that the distributions of all wind-speed fluctuations are non-Gaussian except for the time 1000–1200 PST for sonic data and for the time 1200–1400 PST for LES data. Similarly, the kurtosis, in general, decreases as time advances for both LES and sonic data. The larger kurtosis values indicate more fluctuations of the variable, indicating downdrafts and updrafts with higher vertical velocity in the given area. Furthermore, the p.d.f. becomes more symmetrical over the time from 1000 to 1600 PST

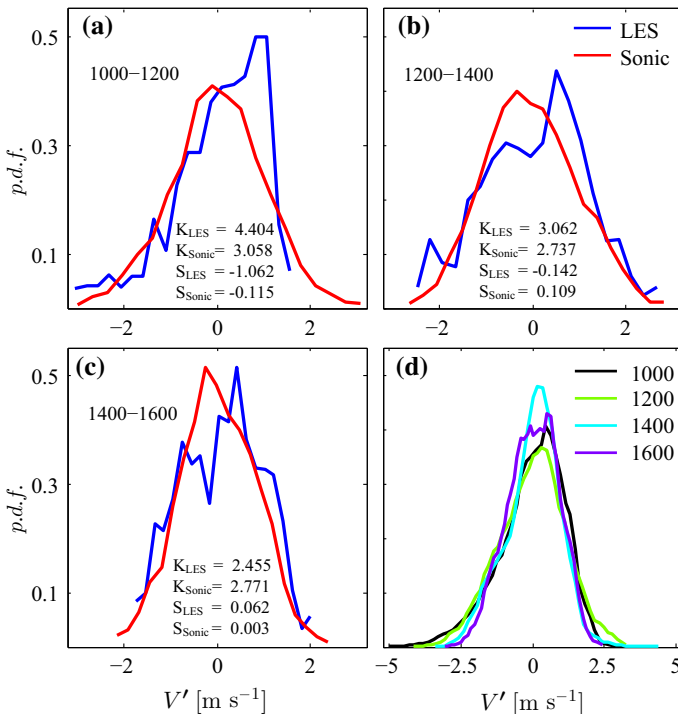


Fig. 11 Probability density function (p.d.f.) constructed using time series for three periods **a** 1000–1200 PST, **b** 1200–1400 PST, and **c** 1400–1600 PST for simulated and observed wind-speed fluctuations at location **c**. Letters *K* and *S* denote the kurtosis and skewness. **d** Shows the averaged p.d.f. across the domain at four instantaneous times (in PST) derived from the wind-speed data from model levels 4–8

(see the skewness value in Fig. 11a–c). The results show that there are smaller differences in the simulated and observed kurtosis and skewness over the latter two periods (i.e., 1200–1400 and 1400–1600 PST) than in the first time period (i.e., 1000–1200 PST), indicating similar statistics, such as mean and standard deviation between the simulated and observed datasets. The disparity in the early period can be viewed as the result of roll vortices that are prominent between 1000–1200 PST (Fig. 9) because their relative position can lead to large differences in the distribution of vertical velocity. In addition, there could be issues associated with the spin-up of the turbulence near the boundary of the LES domain. It should also be noted that the difference in the p.d.f.s for all time periods can also be attributed to potential issues with the numerical schemes and parametrization.

The p.d.f.s of both observed and simulated data reveal that there is great variability in the wind speed over 30-min intervals. However, the p.d.f. derived from the time series at a single point cannot represent the variability in space, particularly in a region of complex terrain. To examine the spatial variation of the fluctuating wind speed over the domain, the wind speed derived from all points in the model domain at a given model level for a given instant of time was used to construct an additional set of p.d.f.s. In Fig. 11d, p.d.f.s derived from five model layers (averaged over levels 4 through 8) at four instantaneous times are presented. To avoid effects at the boundary, 23 grid points inside each lateral domain boundary were excluded when the p.d.f. calculation was made. Model layer 5 corresponds to a height ≈ 90 m, which is an approximate height of the hub of a modern utility-scale wind turbine. The results show that the magnitude of fluctuations in the wind speed is reduced as time progresses. For the spatially-distributed mean wind speed, the p.d.f.s are skewed to negative values. This implies that the wind-speed fluctuations are not symmetrical, perhaps due to the complex terrain, numerical artefacts, and forcing function (wind shear and heat flux). The kurtosis of the distribution also changes with time, with the distribution becoming more peaked as time progresses. This change of the kurtosis value is associated with increased levels of turbulence with time, which may be due to the presence of the complex terrain and/or the changes of forcing (i.e., wind shear or buoyancy).

5 Conclusions

A WRF-LES model with 30-m grid spacing has been used to simulate several meteorological variables of importance to turbulent inflow applications in the convective PBL over an area of complex terrain (CBWES site). The aim of using 30-m grid spacing in the LES simulation is to resolve as many of the energy-containing eddies as possible leading to better estimates of the vertical transport of momentum, heat, and moisture within the boundary layer. The simulation results have been evaluated against observations and found in good agreement with regard to the first- and second-order moments as well as the turbulence spectra.

Realistic forcing has been applied at the boundary of the WRF-LES model using WRF-Meso model simulations after a careful selection of grid spacing for use with the mesoscale simulations. For the PBL conditions on the selected day, the results show that using a grid spacing < 1.2 km produces unrealistic oscillating mean wind speed in the mesoscale simulations when using the MYNN PBL scheme—likely associated with induced secondary circulations that were not well resolved in the mesoscale domain. In this case, the study suggests that the smallest grid spacing in the WRF-Meso model should be larger than the PBL depth, which allows for the averaging of eddies within the mesoscale grid cell. In addition, application of a relatively large grid ratio of 5 is used to help prevent the WRF-LES model domain from falling into the grey zone.

The WRF-LES model simulation has revealed the presence of streak-like flow structures (convective rolls), mostly in the late morning when wind speed and heat flux were moderate (7 m s^{-1} and 300 W m^{-2}) in the south-western region of the domain. At the same time, convective cells were found across the ridge in the north-eastern region, which was characterized by lower elevation and low wind speeds. As afternoon progressed, the area occupied by the roll vortices decreased as the wind speed and surface heat flux decreased. It was also observed that the type of flow structures within a microscale domain (e.g., WRF-LES) depended on the distance from the mesoscale inflow boundaries, especially in the outermost domain starting from the late morning and through the afternoon. For example, increasing the microscale domain size reduced the area occupied by the rolls initially and increased the area of open cells. This suggested that the roll vortices could be a numerical artefact if distance from the inflow boundary is not sufficient. However, further experiments and verification using observations must be conducted before drawing firm conclusions. Overall, these results reveal that the turbulent transition from rolls to cells is influenced by the presence of the complex terrain and the forcing (such as wind speed and heat flux) as well as the computational domain size. However, the development of turbulence could be different over areas with different topography (including flat terrain) and/or for other stability conditions, such as the stable PBL.

Analysis of the spatial variability of meteorological variables in regions of complex terrain is useful for understanding the important processes within the PBL. The p.d.f.s of LES and sonic data show the variability in both time and space (e.g., a decrease of kurtosis with time). The resolved fields, such as those analyzed here, can be employed to improve our understanding of boundary-layer processes and to improve the parametrization of boundary-layer turbulence and surface exchange in mesoscale modelling. In addition to improving regional scale simulations, realistic LES results are useful in e.g., wind-energy applications, atmospheric transport and dispersion, wildfire-spread modelling.

Acknowledgements This research was supported by the Office of Energy Efficiency and Renewable Energy of the U.S. Department of Energy as part of the Wind and Water Power Program, and by the Office of Science's Atmospheric Radiation Measurement (ARM) Climate Research Facility. The Pacific Northwest National Laboratory is operated for the DOE by Battelle Memorial Institute under Contract DE-AC05-76RLO1830. A portion of the research was performed using PNNL Institutional Computing at Pacific Northwest National Laboratory.

References

- Aitken ML, Kosović B, Mirocha JD, Lundquist JK (2014) Large eddy simulation of wind turbine wake dynamics in the stable boundary layer using the Weather Research and Forecasting model. *J Renew Sust Energy* 6:033137
- Beare RJ, Macvean MK, Holtslag AAM, Cuxart J, Esau I, Golaz J, Jimenez MA, Khairoutdinov M, Kosović B, Lewellen D, Lund TS, Lundquist JK, McCabe A, Moene AF, Noh Y, Raasch S, Sullivan P (2006) An intercomparison of large-eddy simulations of the stable boundary layer. *Boundary-Layer Meteorol* 118:247–272
- Berg LK, Pekour M, Nelson D (2012) Description of the Columbia Basin Wind Energy Study (CBWES). Technical report PNNL-22036, Pacific Northwest National Laboratory, Richland, Washington, USA
- Beyrich F (1997) Mixing height estimation from sodar data—a critical discussion. *Atmos Environ* 31(23):3941–3953
- Bou-Zeid E, Meneveau C, Parlange MB (2004) Large-eddy simulation of neutral atmospheric boundary layer flow over heterogeneous surfaces: blending height and effective surface roughness. *Water Resour Res* 40:W02505
- Calaf M, Meneveau C, Meyers J (2010) Large eddy simulation study of fully developed wind-turbine array boundary layers. *Phys Fluids* 22:015110

- Chen F, Dudhia J (2001) Coupling an advanced land surface-hydrology model with the penn state-NCAR MM5 modeling system. Part I: model implementation and sensitivity. *Mon Weather Rev* 129:569–585
- Ching J, Rotunno R, Lemone M, Martilli A, Kosović B, Jimenez PA, Dudhia J (2014) Convectively induced secondary circulations in fine-grid mesoscale numerical weather prediction models. *Mon Weather Rev* 142:3284–3302
- Chow FK, Street RL, Xue M, Ferziger JH (2005) Explicit filtering and reconstruction turbulence modeling for large-eddy simulation of neutral boundary layer flow. *J Atmos Sci* 62:2058–2077
- Churchfield MJ, Lee S, Michalakes J, Moriarty PJ (2012) A numerical study of the effects of atmospheric and wake turbulence on wind turbine dynamics. *J Turbul* 13(14):1–32
- Deardorff JW (1972) Numerical investigation of neutral and unstable planetary boundary layers. *J Atmos Sci* 29:91–115
- Grossman RL (1982) An analysis of vertical velocity spectra obtained in the BOMEX fair-weather, trade-wind boundary layer. *Boundary-Layer Meteorol* 23:323–357
- Hong SY, Noh Y, Dudhia J (2006) A new vertical diffusion package with an explicit treatment of entrainment processes. *Mon Weather Rev* 134:2318–2341
- Iacono MJ, Delamere JS, Mlawer EJ, Shephard MW, Clough SA, Collins WD (2008) Radiative forcing by long-lived greenhouse gases: calculations with the AER radiative transfer models. *J Geophys Res* 113(D13103). doi:10.1029/2008JD009944
- Kosović B, Curry JA (2000) A large eddy simulation study of a quasi-steady, stably stratified atmospheric boundary layer. *J Atmos Sci* 57:1052–1068
- LeMone MA (1973) The structure and dynamics of horizontal roll vortices in the planetary boundary layer. *J Atmos Sci* 30:1077–1091
- Lilly DK (1967) The representation of small-scale turbulence in numerical simulation experiments. In: Proceedings IBM scientific computing symposium on environmental sciences, 14–16 Nov, Yorktown Heights, NY
- Liu Y, Warner T, Liu Y, Vincent C, Wu W, Mahoney B, Swerdlin S, Parks K, Boehner J (2011) Simultaneous nested modeling from the synoptic scale to the LES scale for wind energy applications. *J Wind Eng Ind Aerodyn* 99:308–319
- Mason PJ (1989) Large-eddy simulation of the convective atmospheric boundary layer. *J Atmos Sci* 46(11):1492–1516
- Mesinger F, DiMego G, Kalnay E, Mitchell K, Shafran PC, Ebisuzaki W, Jović D, Woollen J, Rogers E, Berbery EH, Ek MB, Fan Y, Grumbine R, Higgins W, Li H, Lin Y, Manikin G, Parrish D, Shi W (2006) North american regional reanalysis. *Bull Am Meteorol Soc* 87(3):343–360
- Mirocha JD, Lundquist JK, Kosović B (2010) Implementation of a nonlinear subfilter turbulence stress model for large-eddy simulation in the advanced research WRF model. *Mon Weather Rev* 138:4212–4228
- Mirocha JD, Kosović B, Aitken ML, Lundquist JK (2014a) Implementation of a generalized actuator disk wind turbine model into the weather research and forecasting model for large-eddy simulation applications. *J Renew Sust Energy* 6:013104
- Mirocha JD, Kosović B, Kirkil G (2014b) Resolved turbulence characteristics in large-eddy simulations nested within mesoscale simulations using the weather research and forecasting model. *Mon Weather Rev* 142:806–831
- Moeng CH (1984) A large-eddy-simulation model for the study of planetary boundary-layer turbulence. *J Atmos Sci* 41(13):2052–2062
- Moeng CH, Sullivan PP (1994) A comparison of shear- and buoyancy-driven planetary boundary layer flows. *J Atmos Sci* 51(7):999–1022
- Moeng CH, Dudhia J, Klemp J, Sullivan P (2007) Examining two-way grid nesting for large eddy simulation of the pbl using the WRF model. *Mon Weather Rev* 135:2295–2311
- Morrison H, Thompson G, Tatarskii V (2009) Impact of cloud microphysics on the development of trailing stratiform precipitation in a simulated squall line: comparison of one- and two-moment schemes. *Mon Weather Rev* 137:991–1007
- Muñoz-Esparza D, Kosović B, Mirocha J, Beek JV (2014) Bridging the transition from mesoscale to microscale turbulence in numerical weather prediction models. *Boundary-Layer Meteorol* 153:409–440
- Nakanishi M, Niino H (2006) An improved Mellor–Yamada level-3 model: its numerical stability and application to a regional prediction of advection fog. *Boundary-Layer Meteorol* 119:397–407
- Noh Y, Cheon WG, Hong SY, Raasch S (2003) Improvement of the K-profile model for the planetary boundary layer based on large eddy simulation data. *Boundary-Layer Meteorol* 107:401–427
- Porté-Agel F, Meneveau C, Parlange MB (2000) A scale-dependent dynamic model for large-eddy simulation: application to a neutral atmospheric boundary layer. *J Fluid Mech* 415:261–284
- Porté-Agel F, Wu Y, Lu H, Conzemius RJ (2011) Large-eddy simulation of atmospheric boundary layer flow through wind turbines and wind farms. *J Wind Eng Ind Aerodyn* 99:154–168

- Rai RK, Gopalan H, Naughton JW (2016) Effects of spatial and temporal resolution of the turbulent inflow on wind turbine performance estimation. *Wind Energy* 19:1341–1354
- Seibert P, Beyrich F, Gryning SE, Joffre S, Rasmussen A, Tercier P (2000) Review and intercomparison of operational methods for the determination of the mixing height. *Atmos Environ* 34:1001–1027
- Skamarock WC (2004) Evaluating mesoscale NWP models using kinetic energy spectra. *Mon Weather Rev* 132:3019–3032
- Skamarock WC, Klemp JB, Dudhia J, Gill DO, Barker DM, Duda MG, Huang XY, Wang W, Powers JG (2008) A description of the advanced research WRF Version 3. Technical report NCAR/TN-475+STR, Mesoscale and Microscale Meteorology Division, National Center for Atmospheric Research, Boulder, Colorado, USA
- Stull RB (1988) An introduction to boundary layer meteorology, vol 13. Springer, New York
- Sykes RI, Henn DS (1989) Large-eddy simulation of turbulent sheared convection. *J Atmos Sci* 46(8):1106–1118
- Talbot C, Bou-Zeid E, Smith J (2012) Nested mesoscale large-eddy simulations with WRF: performance in real test cases. *J Hydrometeorol* 13:1421–1441
- Weckwerth TM, Wilson JW, Wakimoto RM, Crook NA (1997) Horizontal convective rolls: determining the environmental conditions supporting their existence and characteristics. *Mon Weather Rev* 125:505–526
- Wyngaard JC (2004) Toward numerical modeling in the “Terra Incognita”. *J Atmos Sci* 61:1816–1826
- Yang Q, Berg LK, Pekour M, Fast JD, Newsom RK, Stoelinga M, Finley C (2013) Evaluation of WRF-predicted near-hub-height winds and ramp events over a Pacific Northwest site with Complex Terrain. *J Appl Meteorol Clim* 52:1753–1763
- Zhou B, Simon JS, Chow FK (2014) The convective boundary layer in the Terra Incognita. *J Atmos Sci* 71:2545–2563